J. Fluid Mech. (2008), *vol.* 608, *pp.* 71–80.
doi:10.1017/S002211200800222X Printed in the United Kingdom

Steady streaming within a periodically rotating sphere

RODOLFO REPETTO[1,2], JENNIFER H. SIGGERS[2] AND ALESSANDRO STOCCHINO[3]

[1]Department of Engineering of Structures, Water and Soil, University of L'Aquila, Italy

[2]Department of Bioengineering, Imperial College London, UK

[3]Department of Constructions and Environmental Engineering, University of Genoa, Italy

(Received 20 March 2008 and in revised form 13 May 2008)

We consider the flow in a spherical chamber undergoing periodic torsional oscillations about an axis through its centre, and analyse it both theoretically and experimentally. We calculate the flow in the limit of small-amplitude oscillations in the form of a series expansion in powers of the amplitude, finding that at second order, a steady streaming flow develops consisting of two toroidal cells. This streaming behaviour is also observed in our experiments. We find good quantitative agreement between theory and experiments, and we discuss the dependence of the steady streaming behaviour as both the oscillation frequency and amplitude are varied.

1. Introduction

In this paper, we shall consider flow in a sphere undergoing torsional oscillations. Such oscillations are known to produce steady streaming, defined as the time average of a fluctuating flow. This work is motivated by the study of the flow in the vitreous humour of the eye during saccadic rotations of the eyeball, i.e. rapid movements of short duration. When large quantities of a drug are required to be delivered to the retina, intra-vitreal injection is often the most satisfactory method (Xu *et al.* 2000). The drug particles are subsequently advected and diffused around the vitreous humour, and any steady streaming plays an important role in the advection over long times (Riley 2001). In healthy young subjects, the vitreous body has the consistency of a gel and undergoes little movement with eye rotations. However, typically, with advancing age a progressive collapse of the collagenous framework occurs, leading to the liquefaction of the vitreous body (synchysis). Under these circumstances advection is thought to be by far the most important transport process in the vitreous cavity (Maurice 2001). Advection might also play an important role in vitrectomized eyes in which the vitreous is replaced by tamponade fluids, typically silicone oils.

A number of workers have examined steady streaming flows. Classic examples include acoustic streaming (Riley 2001), such as the quartz wind caused by an ultra-high-frequency sound beam, Rayleigh streaming near to a solid boundary and oscillatory pipe flow (Lyne 1971). The phenomenon of steady streaming was reviewed by Riley (1967) who discussed flows around a solid body in an infinite fluid bath performing periodic prescribed translational oscillations. The flow is governed by two dimensionless parameters, the amplitude ε and the Womersley number α (proportional to the square root of the oscillation frequency). At leading order in the limit of small-amplitude oscillations, the dominant balance is between the time-dependent inertial term and the viscous term, giving rise to a velocity field that varies sinusoidally in time.

At next order, the convective inertial terms drive a steady streaming contribution to the solution. This steady streaming has an associated streaming Reynolds number, equal to εRe, where Re is the conventional Reynolds number, defined as $\varepsilon\alpha^2$. Riley (1967) showed that asymptotic techniques can be adopted to study the steady streaming characteristics.

Riley (2001) also discussed torsional oscillations of a body in an infinite fluid bath about its axis. If the body is cylindrical there is no steady streaming, but Gopinath (1993) showed analytically that for an oscillating sphere at high Womersley numbers, a thin Stokes layer is formed at the surface of the sphere, and that outside this there is steady streaming from the poles of the sphere to the equator. For large values of the streaming Reynolds number, a radial jet of fluid is ejected at the equator. This system was also investigated experimentally and numerically by Hollerbach *et al.* (2002) for large Womersley numbers.

The motion of the vitreous humour owing to eyeball rotations has already been studied by David *et al.* (1998). They considered a sphere filled with a viscoelastic fluid undergoing small-amplitude oscillations, and calculated the leading-order azimuthal flow, though not the steady streaming. They also performed a few fully numerical simulations assuming a Newtonian fluid and observed the generation of a steady streaming. Dyson *et al.* (2004) also studied the flow within a periodically rotating sphere in the limit of small-amplitude oscillations. At second order, they argued by inspection of the governing equations that a steady streaming was expected to form, but did not solve the problem. However, they considered the case of large Womersley number and found that a boundary layer forms at the surface of the sphere that drives the steady streaming in the interior. They derived the flow in the boundary layer analytically. Steady streaming in a sphere was also observed through flow visualizations by Repetto, Stocchino & Cafferata (2005). This flow consists of two circulation cells, one in each hemisphere, along which fluid particles close to the equatorial plane move towards the centre, then towards the poles close to the axis of rotation and finally back again close to the wall towards the equator. The above contributions merely provide a qualitative description of the steady streaming in a sphere and, in particular, do not investigate the dependence of the streaming intensity and the circulation cell shape on the controlling parameters.

We study this problem in the case of a sphere filled with a Newtonian fluid. In § 2, we derive and solve the governing equations to find an analytical expression for the leading-order contribution to the steady streaming in the limit of small-amplitude oscillations. Then in § 3, we describe the experimental set-up and procedure for data analysis. The theoretical and experimental results are presented and compared in § 4, and a discussion follows in § 5.

2. Formulation of the problem and solution

We consider a hollow sphere performing torsional periodic rotations about an axis passing through its centre. The sphere is filled with a Newtonian fluid which is set in motion by the domain rotations. The dimensionless governing equations and no-slip boundary conditions for the velocity $\boldsymbol{u}$ and pressure p are derived from the Navier–Stokes and continuity equations, and read:

$$\alpha^2 \frac{\partial}{\partial t}\boldsymbol{u} + \alpha^2 \boldsymbol{u}\cdot\nabla\boldsymbol{u} + \nabla p - \nabla^2\boldsymbol{u} = 0, \quad \nabla\cdot\boldsymbol{u} = 0, \tag{2.1a}$$

$$u = v = 0, \quad w = \varepsilon \sin\vartheta \sin t \quad (r = 1), \tag{2.1b}$$

where t denotes time, ε the amplitude (in radians) of the domain rotations and (u, v, w) the velocity components, expressed in spherical polar coordinates (r, ϑ, φ) (which denote the radial, zenithal and azimuthal directions, respectively). The following scalings from the corresponding dimensional quantities have been adopted

$$\boldsymbol{u} = \frac{\boldsymbol{u}^*}{\omega_0 R_0}, \quad t = t^* \omega_0, \quad r = \frac{r^*}{R_0}, \quad p = \frac{p^*}{\mu \omega_0}, \tag{2.2}$$

where ω_0 denotes the angular frequency of the domain oscillations, R_0 the sphere radius and μ the dynamic viscosity of the fluid. Moreover, we have introduced the Womersley number of the flow which characterizes the frequency, defined as $\alpha = \sqrt{R_0^2 \omega_0 / \nu}$, with ν the kinematic viscosity of the fluid. In the limit of large α, the Womersley number is the ratio between the radius of the sphere and the thickness of the boundary layer at the wall. The flow is governed by the two dimensionless parameters α and ε. We assume ε to be small and seek an axisymmetric (φ-independent) solution of the problem of the form

$$\boldsymbol{u} = \varepsilon \boldsymbol{u}_1 + \varepsilon^2 \boldsymbol{u}_2 + O(\varepsilon^3), \quad p = \varepsilon p_1 + \varepsilon^2 p_2 + O(\varepsilon^3). \tag{2.3}$$

The solution we will develop is valid for any value of the Womersley number α, and therefore for any value of the streaming Reynolds number. Note that most types of eye rotations have small amplitude, for example, reading has typical value of ≈ 0.15 rad (see Dyson *et al.* 2004). Values of α vary widely, from order 1 to a few hundreds, as both the frequency and the viscosity of the fluid may change over several orders of magnitude.

2.1. *Order* ε^1

In (2.1) the equations for the radial and zenithal components, u_1 and v_1, of $\boldsymbol{u}_1$ and the pressure, p_1, decouple from the equation for the azimuthal component w_1. Since the equations and boundary conditions for u_1, v_1 and p_1 are homogeneous, the solution is $u_1 = v_1 = 0$ and p_1 is constant, whilst w_1 satisfies

$$\frac{\partial w_1}{\partial t} = \frac{1}{\alpha^2}\left[\frac{1}{r^2}\frac{\partial}{\partial r}\left(r^2 \frac{\partial w_1}{\partial r}\right) + \frac{1}{r^2 \sin\vartheta}\frac{\partial}{\partial \vartheta}\left(\sin\vartheta \frac{\partial w_1}{\partial \vartheta}\right) - \frac{w_1}{r^2 \sin^2\vartheta}\right], \tag{2.4}$$

$$w_1 = \sin\vartheta \sin t \qquad (r = 1), \tag{2.5}$$

which has solution

$$w_1 = g_1(r) \mathrm{e}^{\mathrm{i}t} \sin\vartheta + \text{c.c.}, \quad g_1(r) = -\frac{\mathrm{i}}{2r^2}\left(\frac{\sin kr - kr\cos kr}{\sin k - k\cos k}\right), \quad k = \mathrm{e}^{-\mathrm{i}\pi/4}\alpha, \tag{2.6}$$

where c.c. denotes the complex conjugate.

In figure 1, we show azimuthal velocity profiles on the equatorial plane ($\vartheta = \pi/2$) at different times for two different values of the Womersley number α. In the limit $\alpha \to 0$, profiles of w_1 tend to become straight lines, which corresponds to rigid-body flow, whereas at large values of α, an oscillatory boundary layer forms at the wall, and there is no leading-order motion in the interior.

2.2. *Order* ε^2

We decompose the terms into their time harmonics by setting

$$\left.\begin{aligned} \boldsymbol{u}_2 &= \boldsymbol{u}_{20} + \left\{\boldsymbol{u}_{22}\mathrm{e}^{2\mathrm{i}t} + \text{c.c.}\right\}, \quad p_2 = p_{20} + \left\{p_{22}\mathrm{e}^{2\mathrm{i}t} + \text{c.c.}\right\}, \\ \boldsymbol{u}_1 \cdot \nabla \boldsymbol{u}_1 &= \mathscr{F}_0 + \left\{\mathscr{F}_2 \mathrm{e}^{2\mathrm{i}t} + \text{c.c.}\right\}, \end{aligned}\right\} \tag{2.7}$$

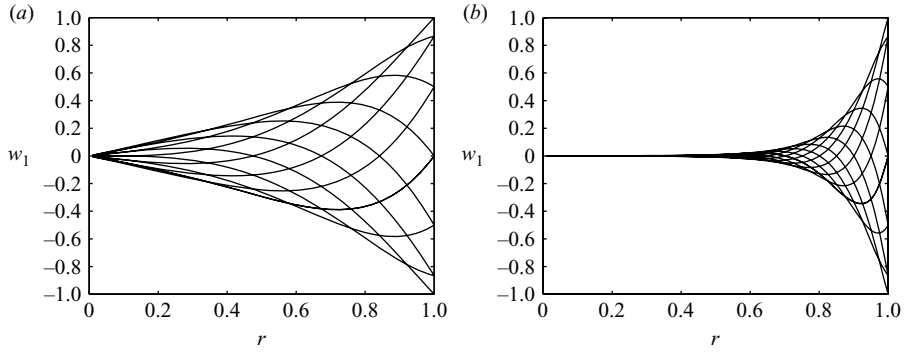

FIGURE 1. Order ε solution. Azimuthal velocity profiles on the plane $\vartheta = \pi/2$ at different times. (*a*) $\alpha = 5$, (*b*) $\alpha = 15$.

where $\boldsymbol{u}_{20}$, $\boldsymbol{u}_{22}$, p_{20}, p_{22}, $\mathscr{F}_0$ and $\mathscr{F}_2$ are independent of time. The leading-order contribution to the steady streaming is given by $\boldsymbol{u}_{20}$, and therefore we neglect $\boldsymbol{u}_{22}$, p_{22} and $\mathscr{F}_2$ in this analysis. The steady component of (2.1) at order ε^2 is

$$\nabla^2 \boldsymbol{u}_{20} - \nabla p_{20} = \alpha^2 \mathscr{F}_0, \quad \nabla \cdot \boldsymbol{u}_{20} = 0, \tag{2.8a}$$

$$u_{20} = v_{20} = w_{20} = 0, \quad (r = 1), \tag{2.8b}$$

Following the approach used by Quartapelle & Verri (1995), we expand all terms as a sum of vector spherical harmonics, which are given by

$$\boldsymbol{P}_n^m(\vartheta, \varphi) \equiv \hat{\boldsymbol{r}}(\vartheta, \varphi) Y_n^m(\vartheta, \varphi) \quad (n \geqslant 0), \tag{2.9a}$$

$$\boldsymbol{B}_n^m(\vartheta, \varphi) \equiv \frac{1}{s_n} r \nabla Y_n^m(\vartheta, \varphi), \quad \boldsymbol{C}_n^m(\vartheta, \varphi) \equiv \frac{1}{s_n} \nabla \times [\boldsymbol{r}(\vartheta, \varphi) Y_n^m(\vartheta, \varphi)] \quad (n > 0), \tag{2.9b}$$

for $-n \leqslant m \leqslant n$, and $Y_n^m(\vartheta, \varphi)$ denotes the normalized spherical harmonic; in particular, $Y_n^0(\vartheta, \varphi) = \sqrt{(2n+1)/(4\pi)} P_n(\cos\theta)$, where P_n is the nth Legendre polynomial (see for instance Arfken & Weber 2001) and $s_n = \sqrt{n(n+1)}$. For any pair m and n, the vectors $\boldsymbol{P}_n^m$, $\boldsymbol{B}_n^m$ and $\boldsymbol{C}_n^m$ are mutually orthogonal; $\boldsymbol{P}_n^m$ is radial, whilst $\boldsymbol{B}_n^m$ and $\boldsymbol{C}_n^m$ span the zenithal and azimuthal components, (and $\boldsymbol{B}_n^0$ and $\boldsymbol{C}_n^0$ are a zenithal and azimuthal vector, respectively). The orthogonality conditions satisfied by $\boldsymbol{P}_n^m$, $\boldsymbol{B}_n^m$ and $\boldsymbol{C}_n^m$ are described in detail by Quartapelle & Verri (1995).

Using the orthogonality properties of the vector spherical harmonics, it may be shown that

$$\mathscr{F}_0 = \mathscr{F}_{P0}(r) \boldsymbol{P}_0^0(\vartheta, \varphi) + \mathscr{F}_{P2}(r) \boldsymbol{P}_2^0(\vartheta, \varphi) + \mathscr{F}_{B2}(r) \boldsymbol{B}_2^0(\vartheta, \varphi) \tag{2.10}$$

where

$$\mathscr{F}_{P0} = -\tfrac{8}{3}\sqrt{\pi} \frac{g_1 \overline{g_1}}{r}, \quad \mathscr{F}_{P2} = \tfrac{8}{15}\sqrt{5\pi} \frac{g_1 \overline{g_1}}{r}, \quad \mathscr{F}_{B2} = \tfrac{4}{15}\sqrt{30\pi} \frac{g_1 \overline{g_1}}{r}. \tag{2.11}$$

Owing to the special behaviour of the vector spherical harmonics under vector calculus, operators $\boldsymbol{u}_{20} = (u_{20}, v_{20}, w_{20})$ and p_{20} can be expanded as

$$\boldsymbol{u}_{20} = u_{20,0}(r) \boldsymbol{P}_0^0(\vartheta, \varphi) + u_{20,2}(r) \boldsymbol{P}_2^0(\vartheta, \varphi) + v_{20,2}(r) \boldsymbol{B}_2^0(\vartheta, \varphi), \tag{2.12a}$$

$$p_{20} = p_{20,0} Y_0^0(\vartheta, \varphi) + p_{20,2} Y_2^0(\vartheta, \varphi). \tag{2.12b}$$

Note that the azimuthal velocity component w_{20} vanishes, and velocity vectors of the steady streaming lie on the planes containing the axis of rotation.

By substituting the expansions (2.12) into (2.8), the following ordinary differential problem in r is obtained

$$\frac{\mathrm{d}^2}{\mathrm{d}r^2}u_{20,0}+\frac{2}{r}\frac{\mathrm{d}}{\mathrm{d}r}u_{20,0}-2\frac{u_{20,0}}{r^2}-\frac{\mathrm{d}}{\mathrm{d}r}p_{20,0}=\alpha^2\mathscr{F}_{P0}, \tag{2.13a}$$

$$\tfrac{1}{r^2}\frac{\mathrm{d}}{\mathrm{d}r}(r^2u_{20,0})=0, \tag{2.13b}$$

$$\frac{\mathrm{d}^2}{\mathrm{d}r^2}u_{20,2}+\frac{2}{r}\frac{\mathrm{d}}{\mathrm{d}r}u_{20,0}-8\frac{u_{20,2}}{r^2}+\frac{2\sqrt{6}}{r^2}v_{20,2}-\frac{\mathrm{d}}{\mathrm{d}r}p_{20,2}=\alpha^2\mathscr{F}_{P2}, \tag{2.13c}$$

$$\frac{\mathrm{d}^2}{\mathrm{d}r^2}v_{20,2}+\frac{2}{r}\frac{\mathrm{d}}{\mathrm{d}r}v_{20,2}-\frac{6}{r^2}v_{20,2}+\frac{2\sqrt{6}}{r^2}u_{20,2}-\frac{\sqrt{6}}{r}p_{20,2}=\alpha^2\mathscr{F}_{B2}, \tag{2.13d}$$

$$\frac{\mathrm{d}}{\mathrm{d}r}u_{20,2}+\frac{2}{r}u_{20,2}-\frac{\sqrt{6}}{r}v_{20,2}=0. \tag{2.13e}$$

This system is subject to homogeneous boundary conditions at $r=1$ and regularity conditions at $r=0$.

The solution of (2.13) subject to the boundary conditions is

$$u_{20,0}=0, \tag{2.14a}$$

$$p_{20,0}=P_{20}+\int_0^r -\alpha^2\mathscr{F}_{P0}(r')\,\mathrm{d}r', \tag{2.14b}$$

$$u_{20,2}=c_1r+c_2r^3+rI_1(r)+\frac{1}{r^2}I_2(r)+r^3I_3(r)+\frac{1}{r^4}I_4(r), \tag{2.14c}$$

$$v_{20,2}=\frac{1}{\sqrt{6}}\left(3c_1r+5c_2r^3+3rI_1(r)+5r^3I_3(r)-\frac{2}{r^4}I_4(r)\right), \tag{2.14d}$$

where the pressure is unique up to the arbitrary constant P_{20} (we omit the expression for $p_{20,2}$, which can be immediately computed from (2.13d)), and

$$c_1=-I_1(1)-\tfrac{5}{2}I_2(1)-\tfrac{7}{2}I_4(1),\quad c_2=\tfrac{3}{2}I_2(1)-I_3(1)+\tfrac{5}{2}I_4(1). \tag{2.15}$$

where

$$I_1=-\frac{\alpha^2}{10}\left(r\mathscr{F}_{P2}(r)-2\int_0^r\mathscr{F}_{P2}(r')\,\mathrm{d}r'\right),\quad I_2=\frac{\alpha^2}{10}\left(r^4\mathscr{F}_{P2}(r)-5\int_0^r\mathscr{F}_{P2}(r')r'^3\,\mathrm{d}r'\right), \tag{2.16a,b}$$

$$I_3=\frac{3\alpha^2}{70}\left[\frac{\mathscr{F}_{P2}(r')}{r'}\right]_0^r,\quad I_4=-\frac{3\alpha^2}{70}\left(r^6\mathscr{F}_{P2}(r)-7\int_0^r\mathscr{F}_{P2}(r')r'^5\,\mathrm{d}r'\right). \tag{2.16c,d}$$

In (2.14), the part of the solution which diverges as $r\to 0$ has been eliminated, making use of the regularity boundary conditions at $r=0$.

We then obtain the following expression for the velocity vector $\boldsymbol{u}_{20}$

$$\boldsymbol{u}_{20}=\left(\frac{1}{4}\sqrt{\frac{5}{\pi}}u_{20,2}(3\cos^2\theta-1),\quad -\frac{1}{4}\sqrt{\frac{30}{\pi}}v_{20,2}\cos\theta\sin\theta,0\right), \tag{2.17}$$

and the streamfunction, ψ_{20}, is given by

$$\psi_{20}=\frac{1}{4}\sqrt{\frac{5}{\pi}}r^2u_{20,2}\sin^2\vartheta\cos\vartheta\quad\text{where }\boldsymbol{u}_{20}=\nabla\times\left(\frac{\psi_{20}}{r\sin\vartheta}\hat{\boldsymbol{\varphi}}\right). \tag{2.18}$$

The integrals (2.16) do not admit an analytical solution and have been computed numerically using the recursive adaptive Simpson quadrature method.

In the limit of small α, we may calculate these integrals analytically to find

$$\psi_{20} = \frac{\alpha^6}{415\,800} r^3(1-r^2)^2(2+r^2)\sin^2\vartheta\cos\vartheta + O(\alpha^8), \tag{2.19a}$$

$$\begin{aligned}\boldsymbol{u}_{20} = \frac{\alpha^6}{415\,800}[&r(1-r^2)^2(2+r^2)(3\cos^2\vartheta - 1)\\ &- 3r(1-r^2)(2-3r^2-3r^4)\sin\vartheta\cos\vartheta, 0] + O(\alpha^8),\end{aligned} \tag{2.19b}$$

and thus for small α, the intensity of the steady streaming is proportional to α^6.

On the other hand, for large α, we may approximate $\mathscr{F}_{P2}$ away from the origin as

$$\mathscr{F}_{P2} = \frac{2}{3}\sqrt{\frac{\pi}{5}}\frac{(\alpha^2 r^2 - \sqrt{2}\alpha r + 1)}{r^5(\alpha^2 - \sqrt{2}\alpha + 1)}\mathrm{e}^{-\sqrt{2}\alpha(1-r)} + O(r^{-3}\mathrm{e}^{-\sqrt{2}\alpha}). \tag{2.20}$$

We may evaluate the integrals appearing in (2.16*a–d*) using repeated integration by parts to obtain an infinite series in decreasing powers of α. Hence, we find the leading-order expression for ψ_{20} and $\boldsymbol{u}_{20}$ to be

$$\psi_{20} = \tfrac{1}{8}r^3(1-r^2)\sin^2\vartheta\cos\vartheta + O\left(\tfrac{1}{\alpha}\right), \tag{2.21a}$$

$$\boldsymbol{u}_{20} = \left(\tfrac{1}{8}r(1-r^2)(3\cos^2\vartheta - 1), -\tfrac{1}{8}\left(3r - 5r^3 + \frac{2}{r^3}\mathrm{e}^{-\sqrt{2}\alpha(1-r)}\right)\cos\vartheta\sin\vartheta, 0\right) + O\left(\tfrac{1}{\alpha}\right). \tag{2.21b}$$

The final term in the ϑ-component of $\boldsymbol{u}_{20}$ decays rapidly far from the wall and ensures the no-slip condition is satisfied. This means that the steady streaming flow also has a boundary layer at $r = 1$ for large α. There is no corresponding contribution to the streamfunction ψ_{20}, as it would appear at order $1/\alpha$. Both the above expressions require $r \gg 1/\alpha$, whereas the expressions for ψ_{20} and u_{20} are absorbed into the error term in the boundary layer at the wall for $1 - r \lessapprox 1/\alpha$.

3. Experimental set-up and data analysis

For the present experiments, we employed the apparatus that was described in detail in Repetto *et al.* (2005); the set-up was suitably modified to deal with the specific needs of the present investigation. We briefly recall the characteristics of the main components. The experimental model consists of a spherical cavity of radius equal to 40.8 mm, carved in a Perspex cylinder. The Perspex model is set in rotational motion around its vertical axis by an electrical motor, and for these experiments a periodic sinusoidal temporal law is imposed on the motor shaft.

The working fluid is a 98 % pure glycerol solution, whose refraction index matches that of the Perspex well. This avoids light refraction at the interface between the two materials. The dynamic viscosity of the glycerol solution was measured at the beginning of each experimental run, using a falling ball viscometer. The oscillatory movement of the model was synchronized with a two-dimensional particle image velocimetry (PIV) acquisition system, employed to measure two-dimensional velocity fields.

The acquisition protocol was chosen so as to register a single frame with a sampling rate equal to the frequency of the sinusoidal signal assigned to the motor. This enabled the oscillatory component of the flow to be eliminated and the steady streaming motion to be found directly. Velocity measurements were performed both on the

	Number of runs	ε (rad)	ν (10^{-3} m^2 s^{-1})	f (Hz)	α
Series 1	28	0.0885	1.041 ± 0.010	1–20	3.1–15.9
Series 2	10	0.0442–0.4384	1.161 ± 0.010	2	4.7
Series 3	5	0.0885	1.161 ± 0.010	2–10	4.2–10.5

TABLE 1. Main experimental parameters.

equatorial plane and on a vertical plane. In all cases, the experimental run lasted about 500 periods. The image pairing in our procedure is an integer multiple of the oscillation period, $2\pi/\omega_0$. The recording protocol imposes upper and lower limits on the measurable velocities, restricting the experiments to a fixed range of Womersley numbers for a given amplitude ε: the fact that the shortest time interval of the image pairing is one oscillation period establishes the maximum measurable velocity, whereas too long a time interval leads to an unacceptable percentage of outliers owing to out-of-plane particle loss. At least 450 velocity fields were measured for each run, an ensemble average was performed and the corresponding standard deviations for both velocity components were evaluated, which were found to be at most 5 % of the average velocity. Velocity vectors were then interpolated on a polar grid; finally, for the equatorial plane measurements, an average of the radial velocity component was also performed along the azimuthal direction, φ. The standard deviation value was propagated through the whole post-processing, eventually leading to the value used to plot the error bars shown in the results in § 4.

Three series of experiments were carried out. Velocity measurements on the equatorial plane were performed during the first two series, with the aim of investigating the dependence of the steady streaming on the Womersley number α for an assigned oscillation amplitude ε (series 1) and on the oscillation amplitude for a given Womersley number (series 2). In addition, vertical plane measurements were carried out (series 3) with the goal of investigating the shape of the steady streaming circulation cell. The main experimental parameters are summarized in table 1.

4. Results

In figure 2(*a*), the steady streaming flow predicted by the theory, $\boldsymbol{u}_{20}$, is shown on a plane containing the axis of rotation (z in the figure). This flow consists of a circulation whereby fluid particles close to the equatorial plane move towards the centre of the sphere, then along the axis of rotation towards the poles and back again to the equatorial plane close to the wall. This picture is consistent with the flow visualizations presented by Repetto *et al.* (2005) (see figure 4 of their paper) and numerical simulations performed by David *et al.* (1998). The contour lines show the absolute magnitude of the velocity, which attains its maximum value on the axis of rotation. In figure 2(*b*), the corresponding experimental results are reported. Contour lines refer to the same values of the streaming velocity as in figure 2(*a*). The agreement between theoretical and experimental results is very satisfactory both in terms of the shape of the circulation cell and of the streaming intensity. This is true for all five experiments of series 3.

In figure 3(*a*), the absolute value of the maximum streaming velocity, $|\boldsymbol{u}_{20}|_m$, on the plane $z = 0$ is shown versus the Womersley number. This quantity is a measure of the streaming intensity. The solid curve denotes the theoretical prediction, and experimental results are also reported (series 1 runs) with the corresponding error bars. It appears that the streaming intensity strongly depends on α. In particular

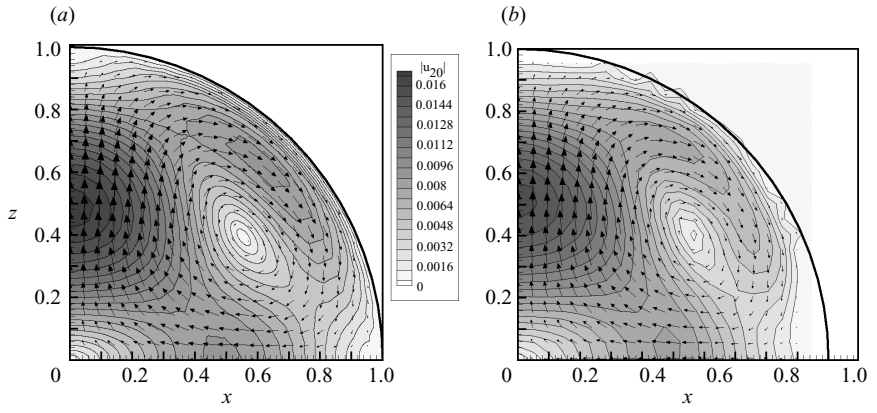

FIGURE 2. Steady streaming circulation cell and contour lines of the absolute value of the velocity on the plane containing the axis of rotation, (*a*) theoretical results, (*b*) experimental measurements from series 1 ($\alpha = 5.1$, $\varepsilon = 0.0885$).

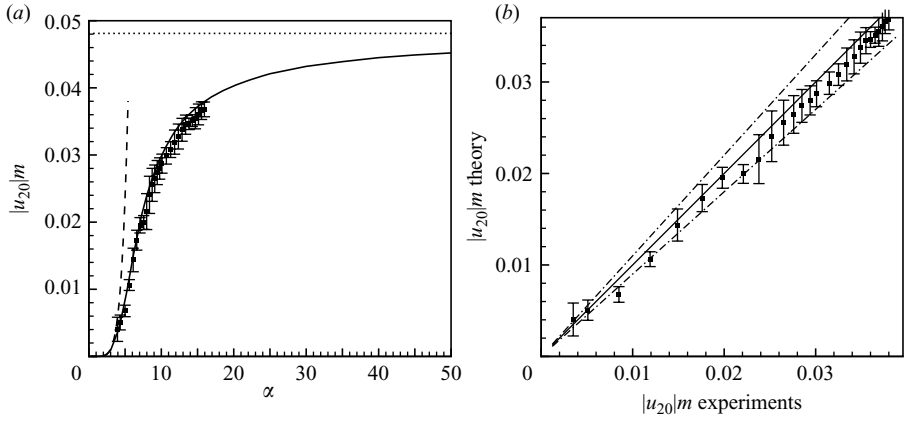

FIGURE 3. (*a*) Streaming intensity versus Womersley number for both theory (solid curve) and series 1 experiments (symbols) with $\varepsilon = 0.0885$. The dashed curve shows the small α limit derived from (2.19*b*); the dotted line shows the large α limit from (2.21*b*). (*b*) Direct comparison of theory and experimental results. The solid line shows an exact match; broken lines indicate errors of $\pm 10\,\%$.

as $\alpha \to 0$, $|\boldsymbol{u}_{20}|_m$ rapidly decreases to small values, consistent with the predicted α^6 scaling (see dashed curve obtained from (2.19*b*)); conversely as α grows, $|\boldsymbol{u}_{20}|_m$ also grows, and tends to the limit $1/(12\sqrt{3})$ (see dotted line and (2.21*b*)).

In figure 3(*b*), theoretical and experimental results are directly compared, showing an overall good agreement. The broken lines at each side of the bisecting line delimit the 10 % error region, and almost all points fall within this band. Note, however, that theoretical predictions consistently slightly overestimate the measured values, which suggests that terms neglected in (2.3) (namely order ε^4 terms) induce a decrease of the streaming velocity.

This speculation is supported by figure 4, where the streaming intensity $|\boldsymbol{u}_{20}|_m$ is plotted versus the amplitude of rotations ε (series 2 experiments). The theoretical curve (solid line) is a parabola (the next correction would be order ε^4). All experimental points lie below the theoretical curve and the departure from the parabolic shape increases as ε grows, as expected, suggesting that order ε^4 terms would probably give

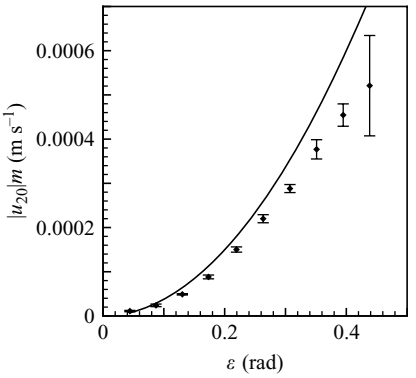

FIGURE 4. Streaming intensity versus oscillation amplitude for both theory (solid curve) and series 2 experiments (symbols) with $\alpha = 4.7$.

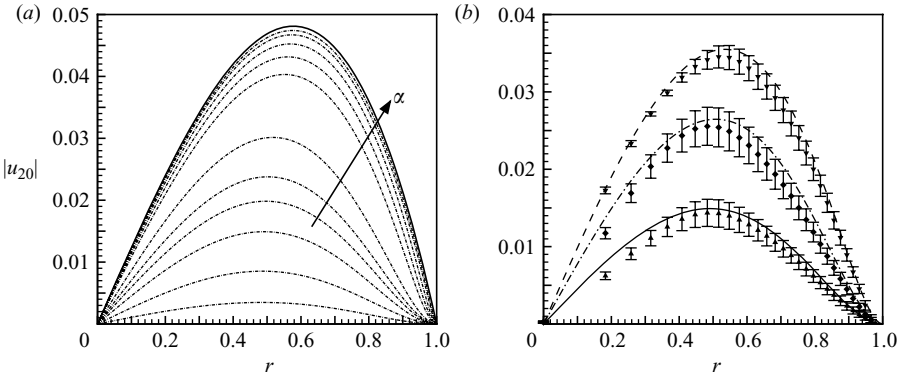

FIGURE 5. Streaming velocity profile on plane $z = 0$. (*a*) Theoretical results for a wide range of α. The thick curve shows the prediction of the asymptotic limit as $\alpha \to \infty$ given by (2.21*b*). (*b*) Comparison of theory and series 3 experiments with $\varepsilon = 0.0885$, and $\alpha = 6.11$ (solid curve and triangle), $\alpha = 8.74$ (dash-dot curve and diamond) and $\alpha = 13.35$ (dashed curve and inverted triangle).

a negative contribution to the steady streaming intensity. Note, however, that the experimental error also grows with ε, as it was more difficult to perform experiments when the streaming intensity was large. This was because for large streaming, the ideal time interval of image pairing is of the same order as the oscillation period; hence fine tuning of this time interval is not possible since the ratio of the two times is restricted to integer values.

Finally, let us analyse in more detail the effect of the value of the Womersley number on the steady streaming pattern. This is done by plotting the radial distribution of the radial component of the streaming velocity in the equatorial plane (figure 5. Again, solid lines denote theoretical results and symbols experimental measurements. It is worth noting that the velocity profile along a radius on the plane $z = 0$ has the same radial structure as that along the axis of rotation, as is apparent from (2.17). Figure 5 shows that the maximum of the velocity profile moves slightly towards the wall as α increases, i.e. the centre of the circulation cell moves outwards, and tends towards the limiting profile obtained from (2.21*b*), shown by the solid curve in figure 5(*a*). Figure 5(*b*) shows that the agreement with the experimental measurements is satisfactory, and indeed we found good agreement for all values of the Womersley number (although, for the sake of clarity, only three profiles are given in the plot).

5. Conclusions and future developments

In this paper we have studied the steady streaming flow generated in a sphere exerting periodic sinusoidal rotations about its axis both theoretically and experimentally. There is good quantitative and qualitative agreement between the experimental and theoretical results. The streaming flow travels from the centre of the sphere towards the poles along the axis, then towards the equator close to the wall before returning towards the centre of the sphere near to the equatorial plane. The streaming intensity, as measured by the maximum speed attained on the equatorial plane, grows as α increases, is proportional to α^6 for small α and tends to a constant value for large α. Thus, for low values of the Womersley number the streaming is weak, suggesting that for high-viscosity fluids the mixing is reduced, which may have implications on the choice of tamponade fluid used after vitrectomy. Finally, there is only a weak dependence of the shape of the steady streaming on the value of α.

The model described here represents a first step in describing the mixing processes occurring during saccadic rotations of the eye. In reality, the vitreous chamber is not a perfect sphere, in particular owing to the presence of the lens which causes an indentation on the anterior side. This effect has been shown to be important in inducing fluid mixing in the vitreous chamber by Stocchino, Repetto & Cafferata (2007). In addition, vitreous humour is normally a viscoelastic fluid. We intend to account for these features in future work.

R. R. and J. H. S. are grateful for funding from the Royal Society International Incoming Short Visits Scheme. J. H. S. also thanks Alistair Fitt, Rosemary Dyson and Oliver Jensen for helpful discussions. R. R. and A. S. thank Giovanni Seminara for providing useful suggestions in the course of the work.

REFERENCES

Arfken, G. B. & Weber, H. J. 2001 *Mathematical Methods for Physicists*, 5th edn. IAP Harcourt Academic Press.

David, T., Smye, S., Dabbs, T. & James, T. 1998 A model for the fluid motion of vitreous humour of the human eye during saccadic movement. *Phys. Med. Biol.* **43**, 1385–1399.

Dyson, R., Fitt, A. J., Jensen, O. E., Mottram, N., Miroshnychenko, D., Naire, S., Ocone, R., Siggers, J. H. & Smith, A. 2004 Post re-attachment retinal re-detachment. In *Proc. Fourth Medical Study Group, University of Strathclyde, Glasgow*.

Gopinath, A. 1993 Steady streaming due to small amplitude torsional oscillations of a sphere in a viscous fluid. *Q. J. Mech. Appl. Maths* **46**, 501–521.

Hollerbach, R., Wiener, R. J., Sullivan, I. S., Donnelly, R. J. & Barenghi, C. F. 2002 The flow around a torsionally oscillating sphere. *Phys. Fluids* **14**(12), 4192–4205.

Lyne, W. H. 1971 Unsteady viscous flow in a curved pipe. *J. Fluid Mech.* **45**, 13–31.

Maurice, D. 2001 Review: practical issues in intravitreal drug delivery. *J. Ocular Pharmacol.* **17**(4), 393–401.

Quartapelle, L. & Verri, M. 1995 On the spectral solution of the three-dimensional Navier–Stokes equations in spherical and cylindrical regions. *Comput. Phys. Commun.* **90**, 1–43.

Repetto, R., Stocchino, A. & Cafferata, C. 2005 Experimental investigation of vitreous humour motion within a human eye model. *Phys. Med. Biol.* **50**, 4729–4743.

Riley, N. 1967 Oscillatory viscous flows. Review and extension. *J. Inst. Maths Applics.* **3**, 419–434.

Riley, N. 2001 Steady streaming. *Annu. Rev. Fluid Mech.* **33**, 43–65.

Stocchino, A., Repetto, R. & Cafferata, C. 2007 Eye rotation induced dynamics of a Newtonian fluid within the vitreous cavity: the effect of the chamber shape. *Phys. Med. Biol.* **52**, 2021–2034.

Xu, J., Heys, J. J., Barocas, V. J. & Randolph, T. W. 2000 Permeability and diffusion in vitreous humor: implications for drug delivery. *Pharmaceut. Res.* **17**, 664–669.